Article

Experimental Study on the Bonding Performance between Shaped Steel and High-Strength Concrete

Qinglin Tao [1] , Weiping Pei [1], Hao Zhang [1], Yi Hu [2], Yuandi Qian [2], Yingtong Wang [1,2] and Zhengyi Kong [1,3,*]

1   Department of Civil Engineering, Anhui University of Technology, Ma'anshan 243032, China; taoqinglin@ahut.edu.cn (Q.T.); 17756264386@163.com (W.P.); 18912961867@163.com (Y.W.)
2   Technology Center, China MCC17 Group Co., Ltd., Ma'anshan 243000, China; tql6551@163.com
3   Institute for Sustainable Built Environment, Heriot-Watt University, Edinburgh EH14 4AS, UK
*   Correspondence: zsh2007@ahut.edu.cn

Abstract: The integration of steel fibers into high-strength concrete (HSC) offers a solution to address the brittleness and limited ductility typically associated with conventional HSC structures. To investigate the bonding properties between shaped steel and high-strength concrete with steel fiber (SFRC), thirteen tests of the shaped steel/SFRC specimens are conducted to explore the effects of various factors such as steel fiber volume ratio, concrete strength grade, reinforcement ratio, steel embedment depth, and cover thickness on bond–slip behavior. Three distinct failure modes, such as pushout failure, bond splitting, and yielding failure of steel, are identified during the pushout tests. Three different types of bond strength, such as the initial bond strength, the ultimate bond strength, and the residual bond strength, are observed from the load–slip curves between the shaped steel and concrete. By incorporating nonlinear spring elements, a numerical model for accurately simulating the bond performance between the shaped steel and SFRC specimens is developed. The bond strength between the shaped steel and concrete increase as the concrete strength, cover thickness, steel fiber volume ratio, and stirrup ratio increase, while it decreases as the steel embedment depth increases. A model for the bond strength between shaped steel and SFRC is developed, and it agrees well with the test data.

Keywords: shaped steel; steel fiber; high-strength concrete; bond strength; finite element analysis

1. Introduction

The steel–concrete composite structure has the characteristics of high bearing capacity and superior seismic performance, and it is widely used in building structures in high-rise and high-intensity seismic areas [1–3]. However, challenges arise regarding ductility when employing high-strength concrete (HSC) in such structures. While HSC can enhance axial and shear bearing capacities, its flexural performance and ductility are often limited [4]. To overcome this limitation, incorporating an appropriate amount of fiber reinforcement material into the concrete matrix is proposed. The micro-reinforcement effect of fibers effectively mitigates concrete crack development and enhances ductility [5–8], thus compensating for the inherent weaknesses of high-strength concrete in terms of ductility and brittleness [9–11].

Currently, some scholars [12–21] have conducted extensive research on steel–concrete materials and components, but the exploration of steel-fiber-reinforced concrete composite structures is relatively scarce. Bui [22] found that reinforced concrete beams reinforced with steel fiber concrete can effectively limit the development of cracks and exhibit good ductility performance. Lin et al. [23] analyzed the failure mechanism of steel-concrete composite beams and found that steel fibers can change the failure mode of steel–concrete composite beams from shear to bending. Wu et al. [24,25] studied the mechanical properties of steel-fiber-reinforced bending members with different steel fiber contents and compared the failure modes of unframed and framed steel-fiber-reinforced bending members, concluding

that the configuration of steel reinforcement can enhance the influence of longitudinal reinforcement on the bearing capacity of steel-fiber-reinforced bending members. Compared with traditional composite structures, steel fibers play a role in transmitting tensile stress in concrete, effectively enhancing the mechanical capacity, ductility, and energy dissipation of the structure.

The bond performance between shaped steel and HSF is an important index for reflecting the steel–concrete composite structures. Previously, Ming et al. [26] studied the bond performance between high-performance concrete with added cellulose fibers and steel and found that the addition of cellulose fibers makes high-performance fiber-reinforced concrete superior to ordinary concrete in terms of toughness and crack resistance. Properly increasing the thickness of the cover thickness and the strength of the concrete can effectively improve the bond strength of high-performance fiber-reinforced concrete. Wukai et al. [27] conducted research on the bond–slip performance between steel and steel-fiber-reinforced concrete and found that with the increase in steel fiber volume ratio, cover thickness, and aspect ratio, the energy loss during specimen slips increases. It was also found that increasing the cover thickness slows down the development of interface cracks in the later stage of the specimen. He et al. [28] analyzed the influence of two parameters, the replacement rate of recycled coarse aggregate (RCA) and the steel fiber content, on the failure mode and bond–slip mechanical behavior of high-strength fiber-reinforced concrete.

Existing research indicates that the addition of fibers can significantly enhance the bond–slip performance of composite structures. However, current studies primarily focus on the bond performance between shaped steel and reinforced concrete, overlooking the impact of high-strength concrete on the bond performance. To address this gap, this study investigates the bonding performance between shaped steel and high-strength concrete, considering various parameters such as steel fiber content, concrete strength grade, stirrup ratio, steel embedment depth, and concrete cover thickness. Thirteen specimens of HSC were subjected to testing to elucidate the bond–slip mechanism, and a finite element method for estimating the bond–slip mechanism between shaped steel and high-strength concrete is developed. Additionally, a calculation method for determining the bond strength between shaped steel and high-strength concrete is proposed.

2. Experimental Program

2.1. Experimental Design

A total of thirteen specimens of HSC were designed and produced for the experiment, including one reference specimen without steel fibers, to study the effects of concrete strength, cover thickness, steel embedment depth, stirrup ratio, and steel fiber content on the bond–slip performance of the specimens, as shown in Table 1. The cross-sectional dimensions of the specimens are 250 mm × 250 mm, 300 mm × 300 mm, and 350 mm × 350 mm, with heights of 300 mm, 400 mm, 600 mm, and 800 mm, as shown in Figure 1. Concrete grades of C60, C70, and C80 were used, and the embedded steel was Q235 I-beam steel with cross section of 150 mm × 75 mm × 7 mm × 4 mm. The longitudinal reinforcement consisted of four HRB335 steel bars, and the stirrups were all made of HPB300 steel, steel fiber volume ratio.
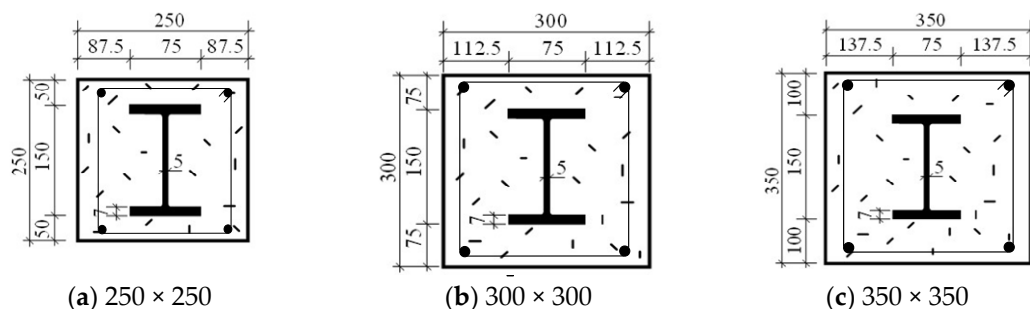

(a) 250 × 250　　　　**(b)** 300 × 300　　　　**(c)** 350 × 350

Figure 1. Cross section of specimens.

Table 1. Details of specimens.

Specimen Number	Concrete Strength Grade (MPa)	Sectional Dimensions (mm²)	Cover Thickness (mm)	Embedded Length (mm)	Hoop Spacing (mm)	Steel Fiber Content (%)
S-1	C60	300 × 300	75	600	100	0.5
S-2	C70	300 × 300	75	600	100	0.5
S-3	C80	300 × 300	75	600	100	0
S-4	C80	300 × 300	75	600	100	0.5
S-5	C80	300 × 300	75	600	100	1
S-6	C80	300 × 300	75	600	100	2
S-7	C80	300 × 300	75	300	100	0.5
S-8	C80	300 × 300	75	400	100	0.5
S-9	C80	300 × 300	75	800	100	0.5
S-10	C80	300 × 300	75	600	80	0.5
S-11	C80	300 × 300	75	600	120	0.5
S-12	C80	250 × 250	50	600	100	0.5
S-13	C80	350 × 350	100	600	100	0.5

2.2. Material Properties

The cubic compressive test is performed to establish the compressive strength of high-strength concrete after 28 days of curing according to CECS13:2009 [29], as shown in Table 2. For example, the cubic compressive strength of C60 concrete with the volume of fiber of 0.5% is 61.9 MPa. Note that the axial compressive strength is also obtained from the relation between the cubic compressive strength and the axial compressive strength provided in CECS13:2009 [29]. The tensile strength of shaped steel and steel reinforcement is also established from the tensile test in line with GB/T 228.1-2021 [30], as shown in Table 3. For example, the yield strength and the ultimate strength of HRB 335 steel reinforcement is 377 MPa and 507 MPa, respectively, and the yield strength and the ultimate strength of the flange of shaped steel is 359 MPa and 547 MPa, respectively.

Table 2. Mechanical properties of high-strength concrete.

Concrete Strength	Volume of Fiber (%)	Cubic Compressive Strength (MPa)	Axial Compressive Strength (MPa)
C60	0.5	61.9	34.2
C70	0.5	72.9	42.5
C80	0	82.3	52.3
C80	0.5	83.3	52.8
C80	1	84.3	53.1
C80	2	84.9	53.2

Table 3. Mechanical properties of shaped steel and reinforcement.

Steel Type	Yield Strength (MPa)	Ultimate Strength (MPa)	Elastic Modulus (GPa)
Flange	359	547	208
Web	350	494	207
HRB335	377	507	221
HPB300	368	457	218

2.3. Loading Scheme

Based on GB/T 50152—2012 [31], the displacement control with a loading rate of 0.1 mm/min was utilized. The load was applied directly to the loading end steel, while a 30 mm thick U-shaped steel plate was placed at the bottom of the concrete, as illustrated in Figure 2. The experiment ceased when the loading end steel penetrated the concrete or the yielding of the steel. Two displacement gauges were situated at the lower loading plate to monitor the relative slip between the shaped steel and concrete, as depicted in Figure 2.
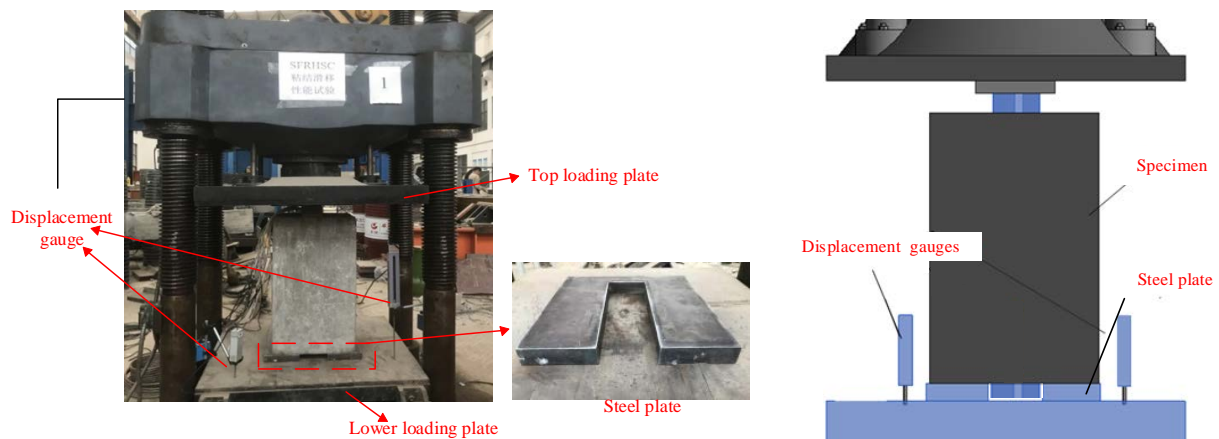
Figure 2. Experimental setup.

3. Experimental Results and Discussion

3.1. Failure Mode

The analysis results revealed that the specimens failed in three different forms: pushout failure (S-1 to S-8), bond-splitting failure (S-11 and S-12), and yielding failure of the steel (S-9, S-10, and S-13), as depicted in Figures 3–5.

3.1.1. Pushout Failure

Initially, the applied load was insufficient to counteract the chemical bonding force between the shaped steel and concrete, resulting in minimal displacement. As the load increased to 30% to 50% of the ultimate load, the displacement gauge began to rise, indicating slight slippage at the loading end, accompanied by the emergence of vertical fine cracks on the concrete surface in the direction of the flange. Upon reaching 80% of the ultimate load, a vertical crack manifested in the middle of the flange direction of the specimen, with two additional vertical cracks extending along the flange tip direction. Finally, the load precipitously dropped, leading to a rapid development of a vertical crack in the middle of the flange direction, traversing the entire specimen.

3.1.2. Bond Splitting Failure

In this type of failure, bond splitting cracks developed at the location of the compressed flange of the shaped steel, featuring vertical cracks at each end of the flange tip extending outward at a 45° angle, along with a vertical crack in the middle of the flange. Vertical cracks on the side only occurred in the concrete at the flange surface, with three vertical cracks originating from the loading end.

The cover thickness of the concrete is a crucial factor affecting the bonding performance between the shaped steel and concrete. Greater cover thickness leads to better bond performance between the shaped steel and concrete.

(**a**) Top view

Figure 3. *Cont.*

(**b**) Side view

(**c**) Bottom view

Figure 3. Pushout failure.

(**a**) Top view

(**b**) Side view

Figure 4. *Cont.*

(**c**) Bottom view

Figure 4. Bond splitting failure.

3.1.3. Yielding Failure of Steel

The failure of steel primarily occurred in specimens with larger concrete cross-sectional dimensions, higher stirrup ratios, and deeper steel embedment. The crack distribution at the loading end of specimens was similar to the other two types of failure modes, featuring a vertical crack in the middle of the flange and a 45° diagonal crack at the flange tip, extending outward from the specimen.

(**a**) Top view

(**b**) Side view


(**c**) Bottom View

Figure 5. Yielding failure of steel.
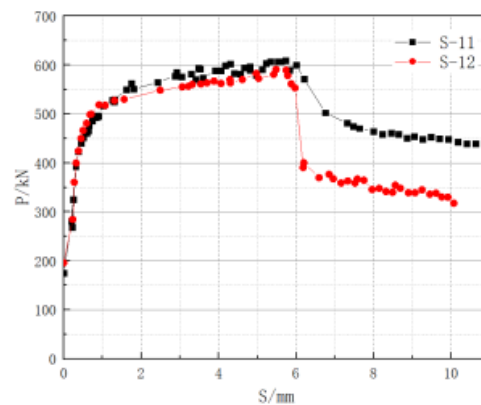
3.2. Load-Slip Curves

The load-slip curves of the loading ends of each specimen are depicted in Figure 6, illustrating three distinct types of P-S curves corresponding to three types of failure modes. Specimens experiencing pushout failure and bond splitting failure exhibit curves comprising an ascending segment, a descending segment, and a horizontal residual segment. In contrast, the P-S curve of specimens undergoing yielding failure comprises only an ascending segment and a horizontal residual segment, with a sudden decrease in load when the load reaches the ultimate load.
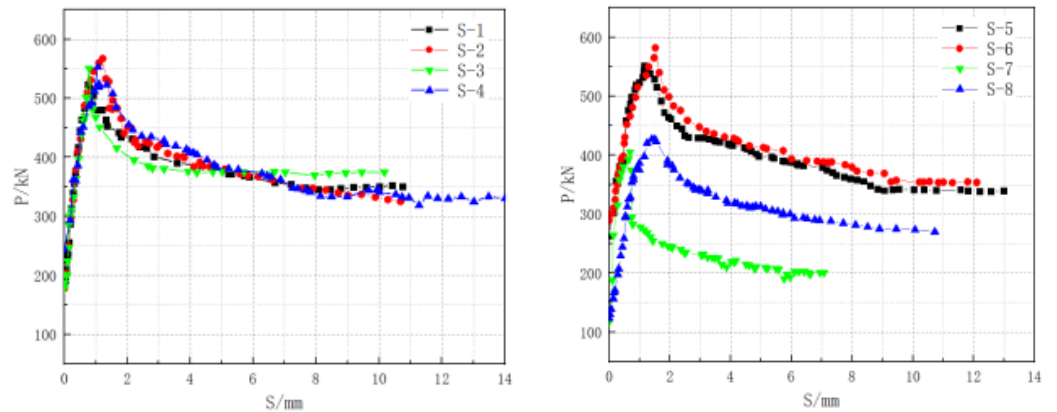
(**a**) Pushout failure
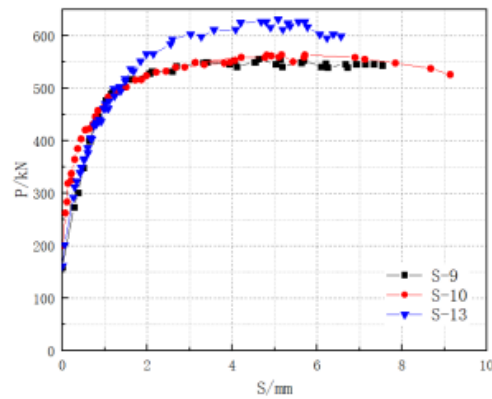
(**b**) Bond-splitting failure

(**c**) Yielding failure of steel

Figure 6. Load–slip curves.

Table 4. Characteristic values of specimens.

Specimen Number	Initial Bond Strength τ_0	Ultimate Bond Strength τ_u	Residual Bond Strength τ_r
S-1	0.328	1.006	0.615
S-2	0.342	1.007	0.626
S-3	0.344	1.06	0.631
S-4	0.471	1.065	0.642
S-5	0.508	1.068	0.655
S-6	0.557	1.121	0.682
S-7	0.453	1.561	0.773
S-8	0.357	1.235	0.781
S-9	0.230	0.778	-
S-10	0.483	1.108	-
S-11	0.367	1.027	0.611
S-12	0.378	1.039	0.631
S-13	0.537	1.103	-

The load–slip curve provides crucial insights into the bond behavior between shaped steel and concrete. Three key parameters can be extracted from this curve: the initial load, the ultimate load, and the residual load.

Initial Load: This represents the onset of slip between the shaped steel and concrete. It signifies the point at which the bond begins to degrade and slip initiates.

Ultimate Load: This is the maximum load sustained by the bond before failure occurs. It indicates the maximum resistance offered by the bond under applied loading conditions.

Residual Load: After reaching the ultimate load, if the bond does not completely fail, a residual load may be sustained. This residual load represents the remaining capacity of the bond after reaching its maximum strength.

These different types of bond strength provide insights into the performance and durability of shaped steel–concrete bonds under varying loading conditions. Table 4 presents these bond strengths corresponding to the initial load, ultimate load, and residual load, facilitating a comprehensive understanding of the bond behavior throughout the loading process.

4. Finite Element Analysis

4.1. Finite Element Method

The model incorporates S4R shell elements for the steel, C3D8R solid elements for the concrete, and T3D2 truss elements for longitudinal and stirrup reinforcements. The mesh size of all specimens is set as 0.02 to achieve convergence and accuracy of the model. Identical with the boundary conditions in the test, the bottom displacement of the concrete is restricted in the X, Y, and Z directions. Additionally, a 50 mm displacement is imposed at the top of the shaped steel along the Z-axis, as depicted in Figures 7 and 8.

(**a**) Shaped steel (**b**) Concrete (**c**) Boundary condition
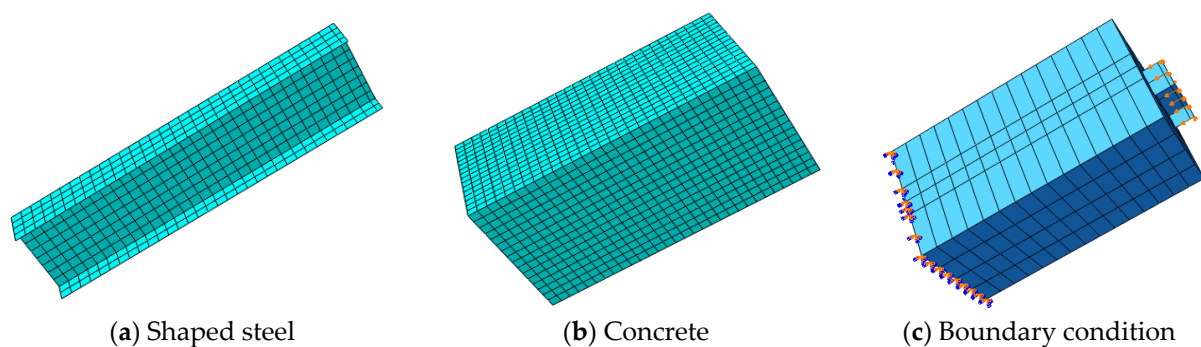
Figure 7. FE model.

Both longitudinal and stirrup reinforcements are embedded within the concrete. To emulate the slip between the shaped steel and concrete, the constitutive model proposed

by Yang [32] for the force–displacement (F-D) curve of the spring element is employed, as shown below (Figure 9):
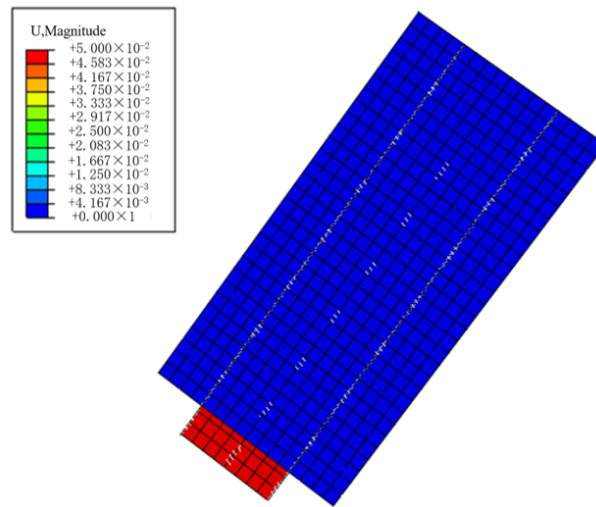

Figure 8. Displacement status of concrete and shaped steel.

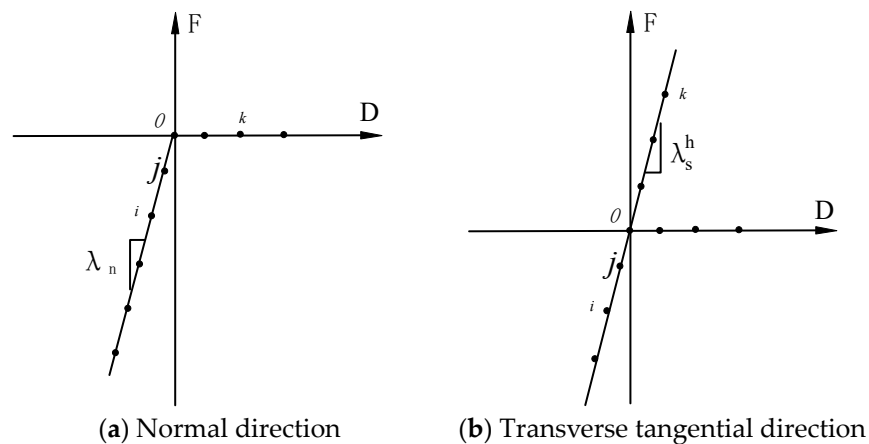(**a**) Normal direction   (**b**) Transverse tangential direction

Figure 9. *F-D* curve of spring.

(1) The interaction in the normal direction is modeled as an equivalent spring with high stiffness designed to bear compressive forces, as shown in Figure 9a.

(2) The web and concrete are solidified in the transverse tangential direction, behaving as a spring with a high stiffness, as shown in Figure 9b.

(3) The interaction in the longitudinal tangential direction is manifested as a bond–slip phenomenon between the shaped steel and concrete, and the mathematical expression of the F-D curve for this spring element is as shown in Equation (1).

$$F = k_{\mathrm{s}}D - \alpha D^n \tag{1}$$

where F is the force, D is the displacement, k_{s} is the stiffness coefficient, α is the slip characteristic, and n is an exponent characterizing the nonlinearity of the bond–slip relationship [32].

4.2. Material Properties

A bilinear elastic–plastic model is selected as the constitutive model of steel [33], as shown in Figure 10 and Equation (2).

$$\sigma_{\mathrm{s}} = \begin{cases} E_{\mathrm{s}}\varepsilon_{\mathrm{s}} & (\varepsilon_{\mathrm{s}} \le \varepsilon_y) \\ f_{\mathrm{y}} & (\varepsilon_y < \varepsilon_{\mathrm{s}} \le \varepsilon_{\mathrm{h}}) \\ f_{\mathrm{y}} + E_{\mathrm{s}}{'}(\varepsilon_{\mathrm{s}} - \varepsilon_{\mathrm{h}}) & (\varepsilon_{\mathrm{s}} < \varepsilon_u) \end{cases} \tag{2}$$

where ε_y is the yielding strain, ε_h is the ultimate strain, ε_u is the fracture strain, E_s is the elastic modulus, E_s' is the plastic modulus, f_y is the yielding strength, and f_u is the ultimate strain.
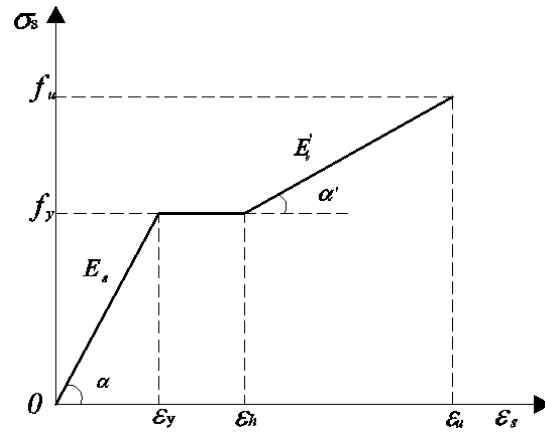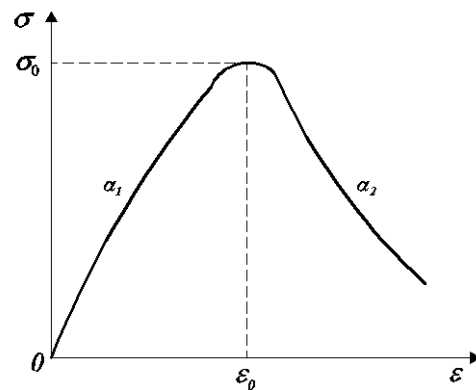

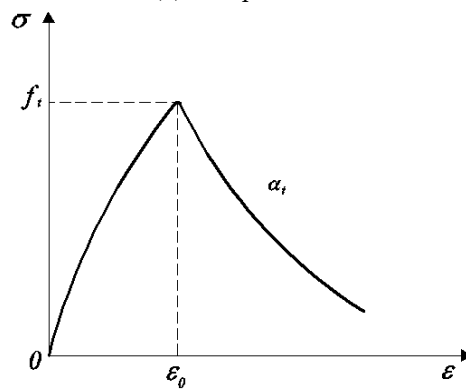**Figure 10.** Stress–strain curve of steel.

For the compressive strength of concrete with steel fiber, the following model is employed [34], as shown in Figure 11.

$$\sigma = \begin{cases} \left[\alpha_1 \frac{\varepsilon}{\varepsilon_0} + (3 - 2\alpha_1) + (\alpha_1 - 2)\left(\frac{\varepsilon}{\varepsilon_0}\right)^3 \right] \sigma_0 & \frac{\varepsilon}{\varepsilon_0} \leq 1 \\ \sigma = \dfrac{\varepsilon/\varepsilon_0}{\alpha_2 \left(\frac{\varepsilon}{\varepsilon_0} - 1\right)^2 + \frac{\varepsilon}{\varepsilon_0}} & \frac{\varepsilon}{\varepsilon_0} > 1 \end{cases} \tag{3}$$

where α_1 and α_2 are the modification coefficients, σ_0 is the ultimate compression strength, and ε_0 is the strain at the ultimate strength.

(**a**) Compression

(**b**) Tension

Figure 11. Stress–strain curve of concrete.

For the tensile strength of concrete with steel fiber, the following model is employed [35], as shown in Figure 11.

$$\sigma = \begin{cases} \dfrac{f_t\left(1.2-0.2\frac{\varepsilon^5}{\varepsilon_0}\right)E_c\varepsilon}{E_c\varepsilon_0} & \varepsilon \leq \varepsilon_0 \\ \dfrac{f_tE_c\varepsilon}{a_tE_c\varepsilon_0\left(\frac{\varepsilon}{\varepsilon_0}-1\right)^{1.7}+\frac{\varepsilon}{\varepsilon_0}} & \varepsilon > \varepsilon_0 \end{cases} \tag{4}$$

where

$$a_t = 0.312\frac{f_t^2}{1+36\lambda_f} \tag{5}$$

$$\varepsilon_0 = 65f_t^{0.54}(1+0.2\lambda_f) \times 10^{-6} \tag{6}$$

$$\lambda_f = v_f\frac{l}{d} \tag{7}$$

where f_t is the tensile strength, a_t is the modification coefficient, E_c is the elastic modulus, ε_0 is the strain at the ultimate stress, and λ_f is the volume ratio of steel fiber.

4.3. Validation of Finite Element Analysis

To verify the finite element method, four specimens (S1, S2, S3, and S7), identical to those in the test, are simulated, as shown in Figure 12. Clearly, the load–slip curves correlate well with the test data. The error of ultimate load estimated from the finite element method is only 5.2%, 9.6%, 6.5%, and 10.2%, respectively. The small differences may be attributed by the micro defects of the concrete in casting. As a result, the finite element method can be used for the estimation of the bond performance between the shaped steel and concrete.
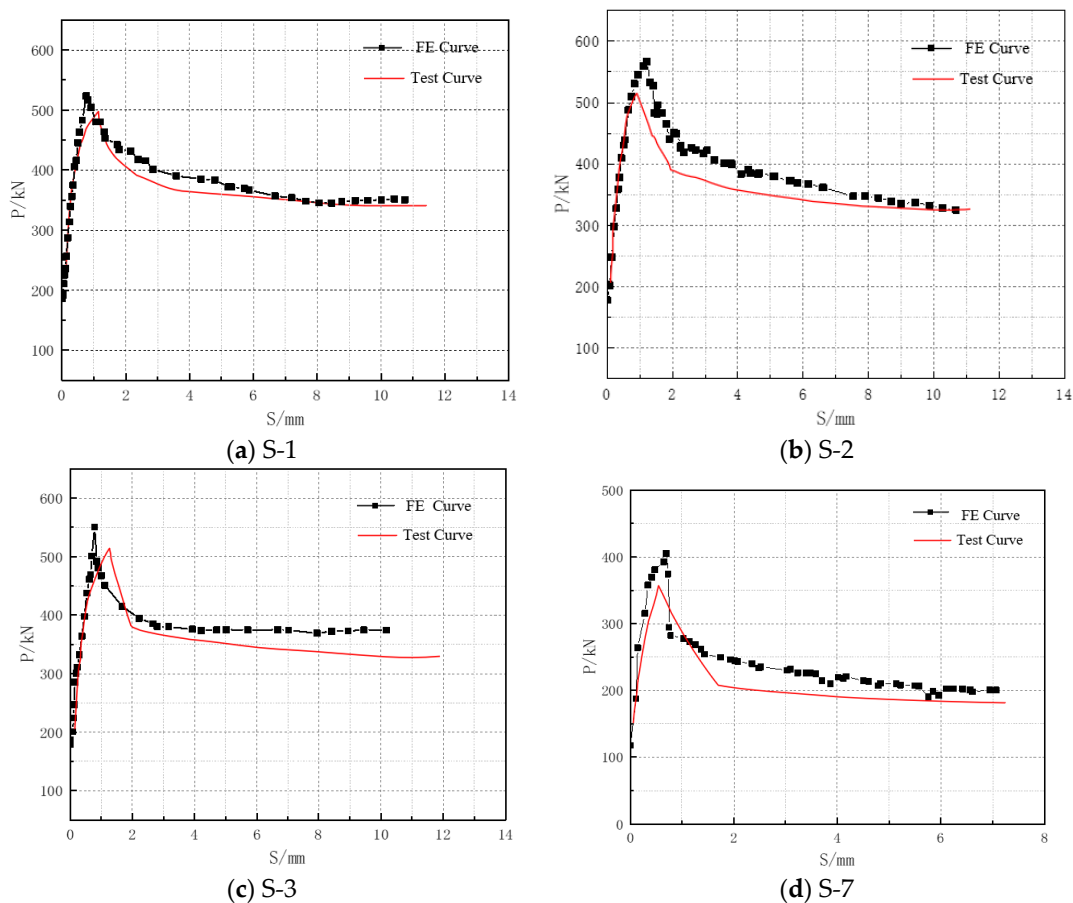

(a) S-1

(b) S-2

(c) S-3

(d) S-7

Figure 12. Comparison of load–slip curves between test and finite element (FE) analysis.

5. Effect of Various Parameters on the Bond Strength

5.1. Concrete Strength

Figure 13 illustrates the correlation between concrete strength and the bond strength between the shaped steel and concrete. The data suggest that concrete strength plays a substantial role in determining the initial bond strength, with higher concrete strength generally resulting in greater initial bond strength. This phenomenon can be attributed to the chemical bonding forces between the shaped steel and the concrete matrix, which tend to increase as the concrete strength increases.

However, as the bond between the shaped steel and concrete is subjected to loading, particularly during testing, the impact of concrete strength on residual bond strength becomes less pronounced. This observation implies that while concrete strength influences the initial bond strength, its effect on the residual bond strength after the specimen reaches ultimate bond strength is relatively minor.
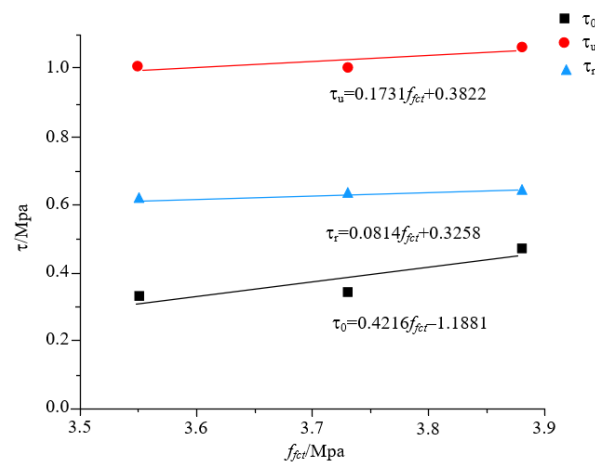

Figure 13. Correlation between bond strength and tensile strength.

5.2. Cover Thickness

Figure 14 depicts the correlation between characteristic bond strength and cover thickness. The data suggest that characteristic bond strength tends to increase as the cover thickness of the steel increases. This trend can be attributed to the greater constraint imposed on the lateral deformation of the shaped steel with increasing cover thickness [28].
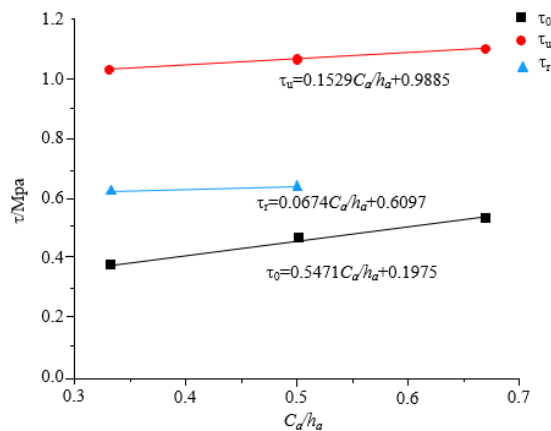

Figure 14. Correlation between bond strength and cover thickness.

As the cover thickness increases, it provides more confinement to the shaped steel, thereby enhancing its resistance to lateral deformation. Consequently, the initial bond strength is most notably affected by variations in cover thickness.

However, while the cover thickness has a significant impact on the initial bond strength, its influence on the ultimate bond strength is comparatively less pronounced. This observation suggests that factors other than cover thickness may become dominant as the bond approaches failure.

5.3. Steel Embedment Depth

Figure 15 depicts the relationship between the steel embedment depth and characteristic bond strength. The data reveal that as the steel embedment depth increases, the anchorage area between the steel and concrete expands, resulting in a corresponding decrease in bond strength. This observed trend can be attributed to the fact that as the embedment depth increases, the average bond strength within the bonding range between the steel and concrete gradually diminishes. While the increased embedment depth augments the anchorage area, it also disperses the bond strength over a larger volume of concrete, thereby reducing the localized bond strength.
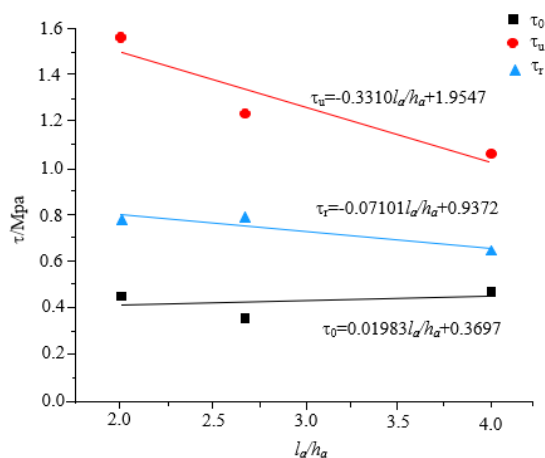

$\tau_u = -0.3310 l_a/h_a + 1.9547$

$\tau_r = -0.07101 l_a/h_a + 0.9372$

$\tau_0 = 0.01983 l_a/h_a + 0.3697$

Figure 15. Correlation between bond strength and steel embedment depth.

5.4. Stirrup Ratio

Figure 16 illustrates the relationship between the characteristic bond strength and the stirrup ratio. The data reveal a consistent linear growth trend in bond strength with increasing stirrup ratio. This phenomenon can be attributed to the role of stirrups in constraining concrete when slip occurs between the steel and concrete interface.
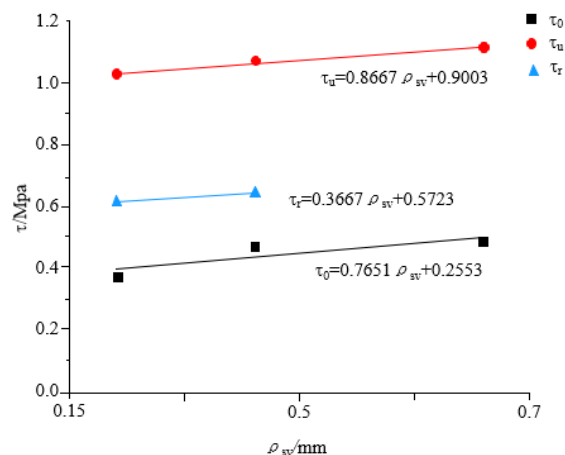

$\tau_u = 0.8667 \rho_{sv} + 0.9003$

$\tau_r = 0.3667 \rho_{sv} + 0.5723$

$\tau_0 = 0.7651 \rho_{sv} + 0.2553$

Figure 16. Correlation between bond strength and steel ratio.

As slip initiates, the stirrups serve to confine the concrete, thereby impeding the expansion of internal voids within the material. As a result, the bond strength experiences

a gradual increase. Upon reaching the ultimate bond stress, the internal voids within the concrete continue to expand. Simultaneously, the restraining effect exerted by the stirrups on both the concrete and steel also intensifies, leading to a substantial increase in ultimate bond strength.

5.5. Steel Fiber Content

Figure 17 illustrates the relationship between steel fiber content and bond strength, highlighting notable trends. It is evident that bond strength increases continuously with rising steel fiber content. This increase is most pronounced in the initial bond strength, with the specimen containing 2% steel fibers exhibiting an initial bond strength approximately 1.5 times that of the specimen without steel fibers. The addition of steel fibers significantly enhances the bonding force at the steel–concrete interface, thereby augmenting the ductility of the specimens and consequently elevating the bond strength.
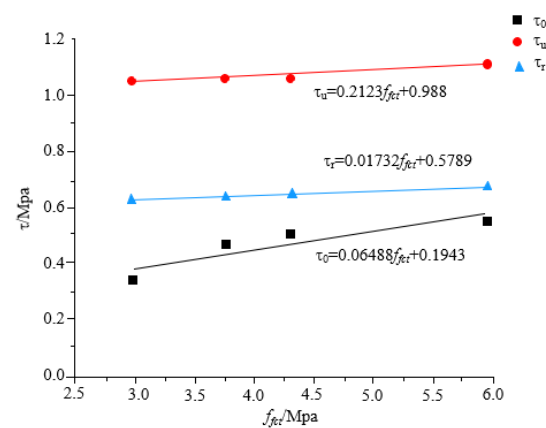

Figure 17. Correlation between bond strength and steel fiber volume fraction.

However, the influence of steel fiber content on residual and ultimate bond strengths is comparatively minor. This is attributed to the formation of cracks within the concrete after slip occurrence, which compromises overall structural integrity. Despite this, bond strength continues to exhibit an upward trajectory.

In summary, the inclusion of steel fibers effectively enhances the bonding force between steel and concrete, resulting in increased ductility and elevated bond strength, particularly in the initial bond strength.

6. Bond Strength

Currently, there are some models for the prediction of the bond strength between shaped steel and reinforced concrete. However, there is a limited model reflecting the influence of high-strength concrete on the bond performance. To derive the bond strength between shaped steel and high-strength concrete, the grey relational analysis theory [36] considering the various factors, such as concrete grade, steel fiber volume fraction, stirrup ratio, cover thickness, and steel embedment depth [26,27], is employed, as shown in Equations (8)–(10).

$$\overline{\tau}_0 = 0.0673 f_t (1 + 1.17\lambda_f) + 0.10942 \frac{C_a}{h_a} + 0.003966 \frac{l_a}{h_a} + 0.15302\rho_{sv} + 0.0012 \tag{8}$$

$$\overline{\tau}_u = 0.034848 f_t (1 + 1.17\lambda_f) + 0.03058 \frac{C_a}{h_a} - 0.066206 \frac{l_a}{h_a} + 0.17334\rho_{sv} + 1.164 \tag{9}$$

$$\overline{\tau}_r = 0.01969 f_t (1 + 1.17\lambda_f) + 0.01348 \frac{C_a}{h_a} - 0.014202 \frac{l_a}{h_a} + 0.07334\rho_{sv} + 0.60479 \tag{10}$$

where $\overline{\tau}_0$ is the initial bond strength; $\overline{\tau}_u$ is the ultimate bond strength; $\overline{\tau}_r$ is the residual bond strength; f_t is tensile strength of concrete; λ_f is the steel fiber characteristic factor; C_a is cover thickness; h_a is web height of shaped steel; l_a is the anchorage length of shaped steel; and ρ_{sv} is the stirrup ratio.

To verify the proposed bond strength, the test data in this work are utilized, as shown in Table 5. Clearly, the suggested models can accurately estimate the bond strength between shaped steel and concrete as the ratio of the test value to the estimated value is 1.096, 1.008, and 1.021, respectively.

Table 5. Comparison of bond strength between calculated and tested values.

Specimen Number	Tested Values			Calculated Values			Tested Value/Calculated Value		
	τ_0/MPa	τ_u/MPa	τ_r/MPa	$\tau'0$/MPa	$\tau'u$/MPa	$\tau'r$/MPa	$\tau_0/\tau'0$	$\tau_u/\tau'u$	$\tau_r/\tau'r$
S-1	0.328	1.006	0.615	0.351	1.071	0.639	0.934	0.939	0.962
S-2	0.342	1.007	0.626	0.363	1.077	0.642	0.942	0.935	0.975
S-3	0.344	1.06	0.631	0.321	1.056	0.630	1.072	1.004	1.002
S-4	0.471	1.065	0.642	0.365	1.078	0.643	1.290	0.988	0.998
S-5	0.508	1.068	0.655	0.402	1.098	0.654	1.264	0.973	1.002
S-6	0.557	1.121	0.682	0.513	1.155	0.686	1.086	0.971	0.994
S-7	0.453	1.561	0.773	0.357	1.211	0.671	1.269	1.289	1.152
S-8	0.357	1.235	0.781	0.359	1.166	0.662	0.994	1.059	1.180
S-11	0.367	1.027	0.611	0.360	1.073	0.640	1.019	0.957	0.955
S-12	0.378	1.039	0.631	0.346	1.073	0.640	1.092	0.968	0.986
Average	-	-	-	-	-	-	1.096	1.008	1.021

7. Conclusions

The pushout tests of thirteen columns of high-strength concrete with steel fiber were performed to investigate the bond–slip behavior between shaped steel and concrete, and the conclusions are as follows:

(1) Three distinct failure modes were identified during the pushout tests: pushout failure, bond splitting, and yielding failure of steel.

(2) The load–slip curves exhibited characteristic features, including an ascending segment, a descending segment, and a horizontal residual segment. Within these segments, three different types of bond strength were observed, reflecting the varying resistance offered by the bond interface at different stages of loading.

(3) Incorporated with the constitutive model of spring element proposed by Yang [32], a finite element model for estimating the bond performance between shaped steel and concrete is developed. The simulation results agree well with the test data.

(4) Increasing concrete strength, cover thickness, steel fiber volume ratio, and stirrup ratio can effectively enhance the bond strength between shaped steel and concrete. However, with the increase in steel embedment depth, except for the initial bond strength increase, it generally exhibits a decreasing trend.

(5) Models for the bond strength between shaped steel and concrete were proposed, and they are in good agreement with the experimental values.

In this work, only thirteen specimens are tested to investigate the bond strength between high-strength concrete and shaped steel, and several parameters (i.e., steel fiber volume ratio, concrete strength grade, reinforcement ratio, steel embedment depth, and cover thickness) are considered in the analysis. Before drawing conclusions regarding engineering structures, such as steel–concrete composite columns in high-rise buildings or steel–concrete composite pier in a bridge, more specimens under different conditions, such as durability and serviceability, should be investigated.

References

1. *Compsite Structure Design*; Higher Education Press: Beijing, China, 2005.
2. Yang, Y.; Xue, Y.C.; Yu, Y.L.; Gao, F.Q. Experimental study on seismic performance of partially precast steel reinforced concrete columns. *Eng. Struct.* **2018**, *175*, 63–75. [CrossRef]
3. Kumar, P.; Patnaik, A.; Chaudhary, S. Effect of bond layer thickness on behaviour of steel-concrete composite connections. *Eng. Struct.* **2018**, *177*, 268–282. [CrossRef]
4. Tao, Q.L.; Niu, B.; Guan, Y.Y.; Kong, J.; Zhang, C.X.; Kong, Z.Y. Experimental and theoretical study on flexural behavior of high strength concrete encased steel beams with steel fibers. *Structures* **2022**, *41*, 1359–1368. [CrossRef]
5. Wei, J.; Ying, H.; Yang, Y.; Zhang, W.; Yuan, H.; Zhou, J. Seismic performance of concrete-filled steel tubular composite columns with ultra-high performance concrete plates. *Eng. Struct.* **2023**, *278*, 115500. [CrossRef]
6. Li, Z.Z.; Zhu, H.T.; Zhen, X.J.; Wen, C.C.; Chen, G. Effects of steel fiber on the flexural behavior and ductility of concrete beams reinforced with BFRP rebars under repeated loading. *Compos. Struct.* **2021**, *270*, 114072. [CrossRef]
7. Pakravan, H.R.; Ozbakkaloglu, T. Synthetic fibers for cementitious composites: A critical and in-depth review of recent advances. *Constr. Build. Mater.* **2019**, *207*, 491–518. [CrossRef]
8. Shan, H.; Zhao, R.; Miao, Y.; Wang, Z.; He, H.; He, C. Effect of carbon dots with different sizes on chloride binding of cement. *Constr. Build. Mater.* **2024**, *425*, 136103. [CrossRef]
9. Tokgoz, S.; Dundar, C. Tests of eccentrically loaded L-shaped section steel fibre high strength reinforced concrete and composite columns. *Eng. Struct.* **2012**, *38*, 134–141. [CrossRef]
10. Zhang, H.K.; Gao, Z.J.; Kong, J.; Ding, W.; Tao, Q.L. Experimental Study on Seismic Behavior of Steel Reinforced High-strength Concrete Column with Steel Fiber. School of Civil Engineering. *Anhui Univ. Technol. Technol. Cent.* **2023**, *40*, 205–212. (In Chinese)
11. Cui, D.; Wang, L.; Zhang, C.; Xue, H.; Gao, D.; Chen, F. Dynamic Splitting Performance and Energy Dissipation of Fiber-Reinforced Concrete under Impact Loading. *Materials* **2024**, *17*, 421. [CrossRef]
12. Zhang, L.F.; Wang, K.; Ling, Z.B.; Omar, A.A.; Guo, K. Bond-slip behavior between reactive powder concrete and H-shaped steel. *J. Constr. Steel Res.* **2023**, *210*, 108058. [CrossRef]
13. Bai, L.; Yu, J.P.; Zhang, M.; Zhou, T.H. Experimental study on the bond behavior between H-shaped steel and engineered cementitious composites. *Constr. Build. Mater.* **2019**, *196*, 214–232. [CrossRef]
14. Ge, H.; Dai, G.L.; Wang, F.; Yu, Y.; Liu, W.S. Theoretical solution for bond-slip behavior of composite structures consisting of H-shape beam and concrete based on experiment, numerical simulation, and theoretical derivation. *Eng. Struct.* **2024**, *302*, 117456. [CrossRef]
15. Ghasemi, M.; Zhang, C.; Khorshidi, H.; Zhu, L.; Hsiao, P. Seismic upgrading of existing RC frames with displacement-restraint cable bracing. *Eng. Struct.* **2023**, *282*, 115764. [CrossRef]
16. Huang, H.; Huang, M.; Zhang, W.; Guo, M.; Liu, B. Progressive collapse of multistory 3D reinforced concrete frame structures after the loss of an edge column. *Struct. Infrastruct. Eng.* **2022**, *18*, 249–265. [CrossRef]
17. Huang, H.; Huang, M.; Zhang, W.; Pospisil, S.; Wu, T. Experimental Investigation on Rehabilitation of Corroded RC Columns with BSP and HPFL under Combined Loadings. *J. Struct. Eng.* **2020**, *146*, 04020157. [CrossRef]
18. Huang, H.; Guo, M.; Zhang, W.; Zeng, J.; Yang, K.; Bai, H. Numerical investigation on the bearing capacity of RC columns strengthened by HPFL-BSP under combined loadings. *J. Build. Eng.* **2021**, *39*, 102266. [CrossRef]
19. Huang, H.; Yuan, Y.; Zhang, W.; Zhu, L. Property Assessment of High-Performance Concrete Containing Three Types of Fibers. *Int. J. Concr. Struct. Mater.* **2021**, *15*, 39. [CrossRef]
20. Huang, H.; Li, M.; Yuan, Y.; Bai, H. Experimental Research on the Seismic Performance of Precast Concrete Frame with Replaceable Artificial Controllable Plastic Hinges. *J. Struct. Eng.* **2023**, *149*, 4022222. [CrossRef]
21. Li, H.; Yuan, Y.; Wang, X.; Tang, H. Effects of the position and chloride-induced corrosion of strand on bonding behavior between the steel strand and concrete. *Structures* **2023**, *58*, 105500. [CrossRef]

22. Bui, L.V.H.; Pitcha, J.; Limpaninlachat, P.; Stitmannaithum, B.; Nguyen, T.T.; Nguyen, T.P. Simulation of shear behavior of corroded reinforced concrete beams flexurally repaired with steel fiber-reinforced concrete. *Structures* **2021**, *34*, 1545–1559.

23. Lin, Y.Z.; Yan, J.C.; Wang, Z.F.; Zou, C.Y. Effects of steel fibers on failure mechanism of S-UHPC composite beams applied in the Arctic offshore structure. *Ocean. Eng.* **2021**, *234*, 109302. [CrossRef]

24. Xu, C.; Wu, K.; Cao, P.Z.; Lin, S.; Chen, Z. Cracking behavior and energy consumption of Steel Fiber Concrete Encased Steel beams. *Adv. Struct. Eng.* **2021**, *24*, 3433–3451. [CrossRef]

25. Wu, K.; Xu, C.; Cao, P.Z. Experimental study on the flexural behavior of profile steel-steel fiber reinforced concrete composite beams. *China Civ. Eng. J.* **2019**, *52*, 41–52. (In Chinese)

26. Ming, M.; Zheng, S.S.; Zheng, H. Experimental study on bond-slip behavior between encased steel and high performance-fiber concrete. *Eng. Mech.* **2020**, *37*, 148–157. (In Chinese)

27. Wu, K.; Chen, F.; Lin, J.F. Experimental study on the interfacial bond strength and energy dissipation capacity of steel and steel fibre reinforced concrete (SSFRC) structures. *Eng. Struct.* **2021**, *235*, 112094. [CrossRef]

28. He, Z.J.; Chen, Y.; Ma, Y.N. The study on bond-slip constitutive model of steel-fiber high-strength recycled concrete. *Structures* **2021**, *34*, 2134–2150. [CrossRef]

29. *CECS13:2009*; Standard Test Methods for Fiber Reinforced Concrete. China Planning Press: Beijing, China, 2010; Volume 4. (In Chinese)

30. *GB/T 228.1-2021*; Metallic Materials—Tensile Testing—Part 1: Method of Test at Room Temperature. Standardization Administration of China:: Beijing, China, 2021; Volume 12. (In Chinese)

31. *GB/T 50152—2012*; Standard for Test Method of Concrete Structures. China Architecture and Building Press: Beijing, China, 2012; Volume 8. (In Chinese)

32. Yang, Y. *Study on the Basic Theory and Its Application of Bond-Slip between Steel Shape and Concrete in SRC Structures*; School of Civil Engineering, Xi'an University of Architectre & Technology: Xi'an, China, 2004. (In Chinese)

33. Robert, W.R.C.C.; Colin, B.B. Shear Connector requirements for Embedded Steel Sections. *J. Struct. Eng. ASCE* **1999**, *125*, 142–151.

34. Yang, W.Z.; Fan, J. A Generic Constitutional Model for Concrete Materials in Axial Compression and Its Application. *J. Zhengzhou Univ. (Eng. Ed.)* **2006**, *27*, 1–4. (In Chinese)

35. Zhang, Y.; LU, X.L.; Nian, X.C. Stress-strain Behavior for High-strength Steel Fiber Reinforced Concrete under Tensile Loading. *Struct. Eng.* **2017**, *33*, 107–113+200. (In Chinese)

36. He, S.; Li, Y.; Wang, R.Z. A new approach to performance analysis of ejector refrigeration system using grey system theory. *Appl. Therm. Eng.* **2009**, *29*, 1592–1597. [CrossRef]